EES Solar

PAPER

View Article Online
View Journal

Cite this: DOI: 10.1039/d6el00010j

HTL- & ETL-free metal–semiconductor–metal structure organic solar cells

Sujung Park,†[a] Hong Nhan Tran,†‡[a] Heunjeong Lee,†[a] Seul Lee,[b] Young Wan Lee,[b] Jin Hee Lee,[c] Jina Roe,[d] Muhammad Jahandar,[e] Nurul Kusuma Wardani,[ei] Jin Young Kim,[df] Jung Hwa Seo,[c] Hoe-Yeon Jeong,[g] Eun-chae Jeon,[g] Young S. Park,[b] Soyeon Kim,[e] BongSoo Kim,*[bfh] Dong Chan Lim*[e] and Shinuk Cho*[a]

Received 27th January 2026
Accepted 3rd February 2026

DOI: 10.1039/d6el00010j

rsc.li/EESSolar

In high-performance organic solar cells (OSCs), the electron transport layer (ETL) and hole transport layer (HTL) are essential for facilitating the efficient transfer of electrons and holes generated in the photoactive layer to the respective electrodes. However, challenges associated with the ETL and HTL remain critical issues in OSC research. In this work, our study presents a novel fabrication approach that eliminates the need for the ETL and HTL, achieving structural simplification while maintaining high performance through simple interfacial treatments between the active layer and electrodes. To implement a Metal–Semiconductor–Metal (MSM) structure without the ETL and HTL, we explored three different approaches. The first strategy (Type-I) used a self-assembled monolayer at the anode interface and a salt for cathode interface modification. The second strategy (Type-II) introduced two different salts at the anode and cathode interfaces, respectively. The third strategy (Type-III) involved simultaneously coating a mixture of hole-transport-capable molecules and active materials to spontaneously form a hole extraction interface, while applying amine salts to the electron-extracting cathode interface. All three approaches successfully achieved OSCs with an MSM structure, yielding performances exceeding 18%, comparable to conventional devices with the ETL and HTL. Our findings offer a substantial simplification in the fabrication process of organic photovoltaic cells, representing a significant advancement toward their commercialization.

Broader context

Although the electron and hole transport layers (ETL and HTL) enhance charge transport in organic solar cells (OSCs), interface challenges remain. Here, we propose a novel fabrication approach that eliminates the ETL and HTL, simplifying the structure while maintaining high performance through interfacial treatments only. To implement a Metal–Semiconductor–Metal (MSM) structure, we explored three strategies. Type-I used a self-assembled monolayer at the anode interface and an amine salt at the cathode interface. Type-II applied different salts at both interfaces. Type-III incorporated a mixture of phosphotungstic acid and active materials for hole extraction while using salt for electron extraction. All strategies successfully achieved MSM-structured OSCs with promising efficiency. This approach significantly streamlines module fabrication, and we successfully fabricated modules in just three steps.

Introduction

In the first organic solar cell (OSC) reported by Ching W. Tang *et al.* in 1986, the photoactive layer was in direct contact with both cathode and anode electrodes without any additional charge extraction layers.[1] At that time, most attention was focused on the composition of the photoactive layer rather than on the contact interface with the electrodes. The photoactive

---

[a] Department of Semiconductor Physics & Engineering and Energy Harvest Storage Research Center, University of Ulsan, Ulsan 44610, Republic of Korea. E-mail: sucho@ulsan.ac.kr

[b] Department of Chemistry, Ulsan National Institute of Science and Technology (UNIST), Ulsan 44919, Republic of Korea. E-mail: bongsoo@unist.ac.kr

[c] Department of Physics, University of Seoul, Seoul 02504, Republic of Korea

[d] Department of Energy Engineering and School of Energy and Chemical Engineering, UNIST, Ulsan 44919, Republic of Korea

[e] Energy & Environment Materials Research Division, Surface Materials Division, Korea Institute of Materials Science (KIMS), Changwon 51508, Republic of Korea. E-mail: dclim@kims.re.kr

[f] Graduate School of Carbon Neutrality, UNIST, Ulsan 44919, Republic of Korea

[g] School of Materials Science and Engineering, University of Ulsan, Ulsan 44776, Republic of Korea

[h] Graduate School of Semiconductor Materials and Device Engineering, UNIST, Ulsan 44919, Republic of Korea

[i] Department of Smart Green Technology Engineering, Pukyong National University, Busan 48513, Republic of Korea

† These authors contributed equally to this work.

‡ Present address: Department of Nano Fusion Technology, Pusan National University, Busan 462412, Republic of Korea.

layer of the first OSC consisted of a bilayer structure of P-type copper phthalocyanine and the N-type perylene tetracarboxylic derivative. However, the power conversion efficiency (PCE) of this initial OSC was quite low (0.95%) due to the limited charge generation and transport to the electrodes. In 1995, Heeger and colleagues introduced the bulk-heterojunction (BHJ) structure into the photoactive layer, significantly increasing the donor–acceptor interface area where excitons are dissociated and reducing the exciton diffusion length, thereby greatly enhancing the PCE.[2]

Alongside the optimization of the photoactive layer morphology to generate sufficient charge, the efficient extraction of these charges to the electrodes is also essential for achieving high PCE. Devices incorporating PEDOT:PSS to improve hole transport properties between ITO and the photoactive layer[3,4] and a thin LiF layer to enhance electron transport between the metal top electrode and the photoactive layer[5,6] have shown significantly improved PCE compared to those with the original metal–semiconductor(photoactive)–metal (MSM) structure. As interface challenges between the photoactive layer and electrodes became apparent, the hole transport layer (HTL) and electron transport layer (ETL) were established as essential components for achieving high-performance OSCs.

Various materials have since been developed and utilized as the HTL and ETL. First, PEDOT:PSS, which has been used since the early stages of OSC research, is still the most widely used HTL material.[7–9] Secondly, metal oxides (*e.g.*, MoO_3, V_2O_5, and NiO for the HTL,[10–12] and ZnO, TiO_2, and SnO_2 for the ETL[13–15]), alcohol-based soluble polymers (*e.g.*, PEI, PEIE, PFN, and CPE complexes),[16–19] and small molecules (*e.g.*, perylene diimide (PDI) derivatives)[20,21] have also been employed. These materials facilitate charge extraction from the photoactive layer to the electrodes, yet the introduction of the ETL and HTL also creates additional interfaces, leading to new interfacial challenges. As a result, issues arising from the ETL and HTL remain critical challenges in OSC research, with non-ohmic contacts often forming between the ITO and transport layer or between the transport layer and top electrode.[22,23]

Even materials considered effective have their own issues. For instance, ZnO, the most common N-type metal oxide for the ETL, can generate oxygen-containing defects that penetrate the photoactive layer, leading to photocatalytic reactions with non-fullerene acceptors (NFAs) under UV light and thus compromising OSC stability. Alcohol-based soluble polymers such as PEI, PEIE, and CPE complexes exhibit low conductivity due to their insulating nature and are sensitive to thickness. Additionally, small molecules such as PDINO and PDINN have limitations, including complex synthesis processes, poor thermal stability, and difficulty forming uniform films due to their planar molecular structures, which tend to form large aggregates during film formation.

PEDOT:PSS, the most widely used and well-established material, faces several stability challenges that significantly affect the performance and lifetime of OSCs. Due to its hydrophilic nature, PEDOT:PSS readily absorbs moisture from the atmosphere, leading to swelling and electrical degradation, thus compromising environmental stability.[24,25] Furthermore, its high acidity (pH ~1.5–2.5) corrodes the indium tin oxide (ITO) electrode, increasing contact resistance and accelerating device deterioration.[25,26] PEDOT:PSS also exhibits limited thermal stability, making it unsuitable for high-temperature applications. At elevated temperatures, phase separation between PEDOT and PSS occurs, reducing conductivity and increasing resistance, thereby accelerating device degradation.[27,28] Additionally, the adhesion of PEDOT:PSS to other layers, particularly electrodes, is often weak, causing delamination and poor mechanical stability.[29] Finally, PEDOT:PSS is highly sensitive to UV radiation and oxygen exposure, resulting in increased resistance and charge trapping, negatively affecting both efficiency and device lifetime.[30,31]

Importantly, in the fabrication of large-area modules, the patterning of the ETL and HTL is essential to prevent intercell contact and lateral transport between sub-cells. Typically, patterning not only involves the use of expensive laser equipment, but also introduces damage protection layers and barriers during the patterning process, making the fabrication process even more complex. Therefore, if modules can be made without an ETL and HTL, the module fabrication process is expected to be greatly simplified.

To ultimately address these issues, it is necessary to implement an OSC with an MSM structure that eliminates the HTL and ETL without sacrificing performance. In this study, we implemented HTL- and ETL-free MSM structure OSCs by employing small molecule salts as interfacial modifiers between the photoactive layer and the electrodes. To achieve the MSM structure, we employed three approaches (see Fig. 1). In quasi-MSM (Type-I) devices, a self-assembled monolayer (SAM) was introduced at the hole-extracting anode interface, while tetrahexylammonium iodide (THA-I) salts were used to modify the electron-extracting interface. In Type-II devices, two different salts, rubidium-tetraphenylborate (Rb-TPB) and THA-I, were used to modify the hole and electron extraction interfaces, respectively. In Type-III devices, phosphotungstic acid (PTA) was mixed into the photoactive material for simultaneous coating, naturally forming the hole extraction interface, while the electron extraction interface was modified with the THA-I salt. Although there were slight variations in performance among the different types, all three types operated effectively without the need for an ETL and/or HTL. Notably, the Type-III method demonstrated robust performance even when conducted on a large scale.

Results and discussion

Type I: Quasi-MSM device with a SAM for holes & N-type salt for electrons

The use of a SAM as a substitute for the hole transport layer in OSCs is a well-established approach, with successful examples reported by numerous researchers. We have demonstrated OSCs with a quasi-MSM structure by introducing THA-I salts into the electron extraction path along with a SAM-based hole extraction layer using 2-(3,7-dibromo-10*H*-phenoselenazine-10-yl)ethyl)phosphonin acid (Br-2EPSe), which has already been proven.[32,33] We named Type-I a quasi-MSM because we were

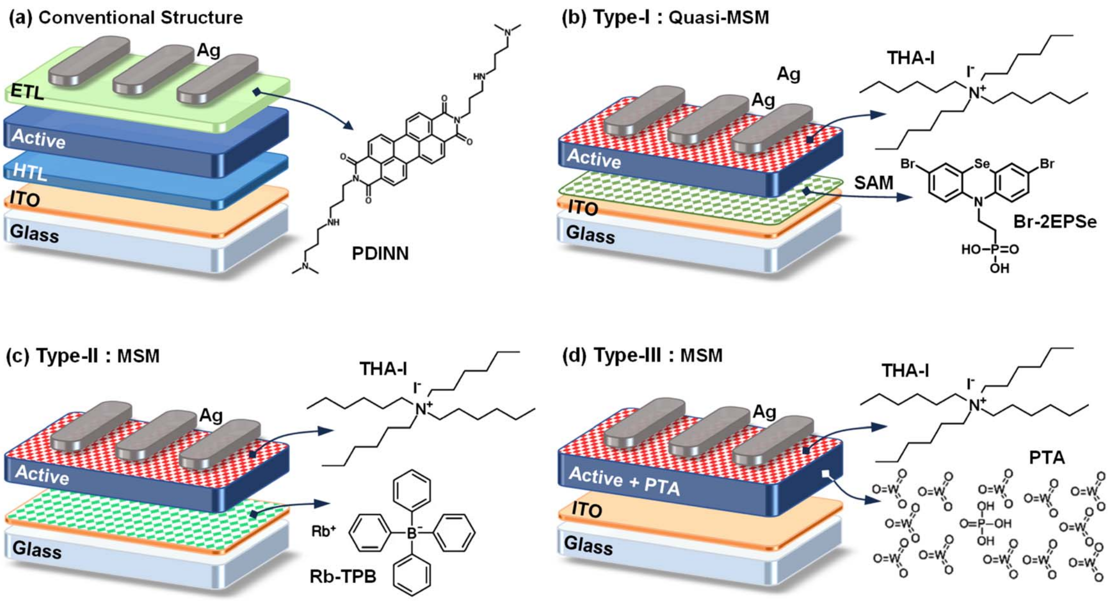

Fig. 1 Three approaches to the Metal–Semiconductor–Metal (MSM) structure. (a) Conventional structure with a HTL and ETL. (b) Type-I: Quasi-MSM with a Br-2EPSe SAM and THA-I N-type salt serving as the hole and electron extraction interfaces, respectively. (c) Type-II: MSM with Rb-TPB P-type salt and THA-I N-type salt serving as the hole and electron extraction interfaces, respectively. (d) Type-III: MSM incorporating a photoactive layer with PTA and THA-I N-type salt.

cognizant of the counterargument that monolayers are also layers. The analysis of SAM-introduced devices has been extensively covered in other literature studies, so we will not go into details here and focus on THA-I only.

THA-I is directly applied on top of the photoactive layer, which consists of PM6:L8-BO (Fig. S1, SI), using a simple spin-coating method. THA-I exhibits good solubility in common alcoholic solvents such as 2-propanol and ethanol. Additionally, it offers a straightforward synthesis route and is readily available at a low cost in the market. Fig. 2a and b presents the current density *versus* voltage (J–V) curves and external quantum efficiency (EQE) curves for the optimized devices, respectively. The PM6:L8-BO control device without an ETL exhibits a maximum PCE of 11.93%, with a short-circuit current (J_{SC}) of 24.865 mA cm^{-2}, an open-circuit voltage (V_{OC}) of 0.766 V, and a fill factor (FF) of 62.51%. For comparison, we fabricated the control device using a perylene diimide derivative, PDINN, which is commonly used as a cathode interlayer in OSCs. The PM6:L8-BO device with PDINN shows improved performance, with a maximum PCE of 18.08%, a J_{SC} of 26.491 mA cm^{-2}, a V_{OC} of 0.877 V, and a FF of 77.75%, which is similar to the results reported for the same device structure (17.98%) in a previous paper.[33] Surprisingly, when THA-I is applied on top of the photoactive layer instead of the ETL, the PCE increases to 18.41%, with a J_{SC} of 26.695 mA cm^{-2}, a V_{OC} of 0.877 V, and a FF of 78.65%. The corresponding device parameters are summarized in Table 1. The use of THA-I was observed to significantly enhance the reproducibility of the devices. Fig. 2c shows the PCE distribution, indicating that while devices using PDINN demonstrate good reproducibility, those using THA-I are distributed within a smaller error range. Of course, we tested various salts with structures similar to THA-I. We experimented with different alkyl chain lengths and ion substitutions (Fig. S2, S3 and Table S1, S2, SI). Among the substances we tested, excluding those that were insoluble in alcoholic solvents or difficult to obtain commercially, THA-I showed the most reliable performance.

To check whether THA-I forms an actual layer on top of the BHJ, we measured whether there was any increase in thickness due to the THA-I treatment. However, no noticeable change was observed (Fig. S4, SI). Atomic force microscopy (AFM) analysis of surface morphology did not reveal any significant differences after THA-I coating (Fig. 2d and f), except for a slight change in surface roughness. In contrast, the sample with a PDINN coating (approximately 5 nm thick), measured for comparison, showed a significantly different surface morphology (Fig. 2e). Although no physical changes indicative of layer formation by THA-I were observed, surface potential changes induced by THA-I were clearly detected in Kelvin probe force microscopy (KPFM) measurements. The surface potential images observed on PM6:L8-BO, PM6:L8-BO/PDINN, and PM6:L8-BO/THA-I films are shown in Fig. 2g–i. The contact potential difference (CPD), initially measured to be 581.6 mV on the PM6:L8-BO surface with the biased cantilever tip as a reference, increased (positively shifted) to 670.8 mV after THA-I treatment. A positive shift in the CPD value indicates a lower Fermi level, while a negative shift suggests a higher Fermi level.[34] Thus, the positive shift in CPD after THA-I treatment reflects a lowered Fermi level on the PM6:L8-BO surface, facilitating electron transport. Compared to PDINN, the narrower surface potential distribution of the PM6:L8-BO film after THA-I treatment demonstrates that THA-I is uniformly distributed across the PM6:L8-BO surface (Fig. 2j).

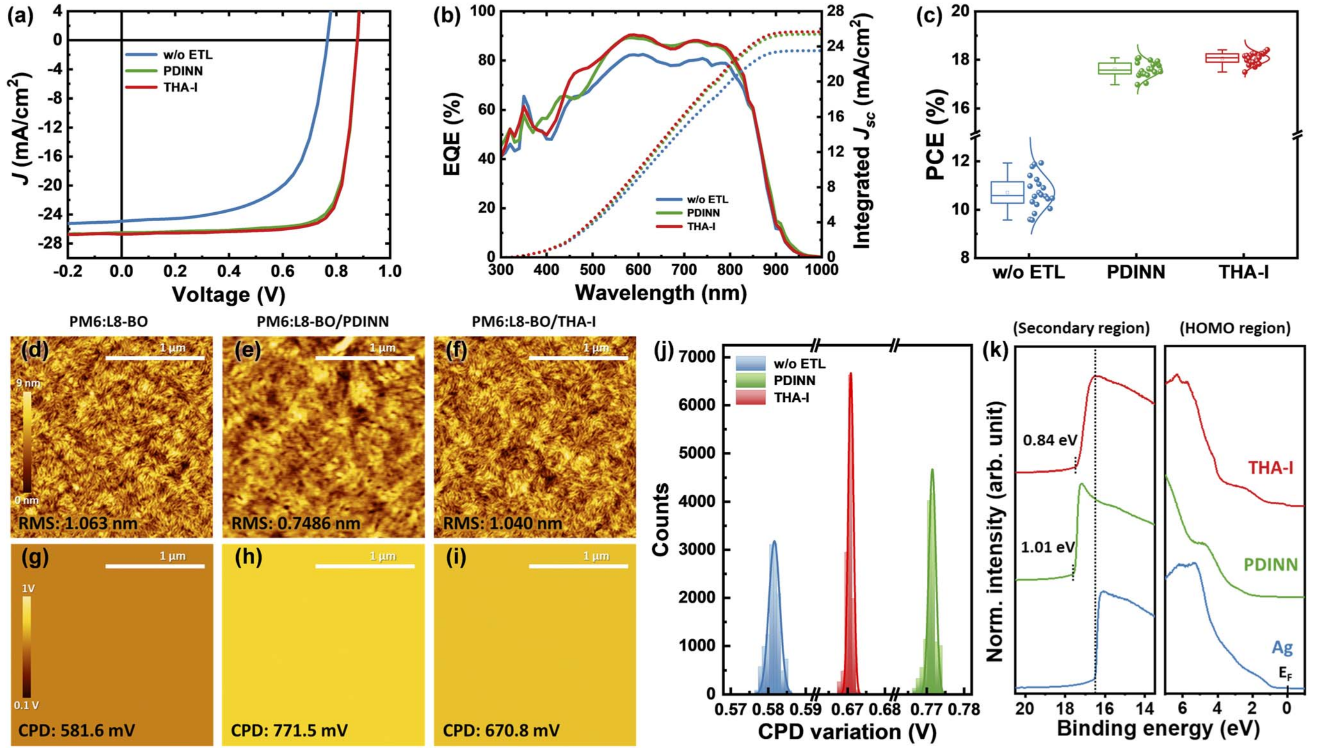

Fig. 2 Photovoltaic performance of Type-I devices and characterization of PDINN ETL and THA-I N-type salt. (a–c) *J*–*V* curves, EQE spectra, and PCE distributions of Type-I devices without an ETL, with PDINN, and with THA-I, measured under AM 1.5 G (100 mW cm^{-2}) illumination, respectively. (d–f) AFM surface morphology images, (g–i) KPFM surface potential images, and (j) contact potential difference measurements of PM6:L8-BO, PM6:L8-BO/PDINN, and PM6:L8-BO/THA-I films, respectively. (k) UPS spectra of Ag coated with PDINN ETL and THA-I N-type salt.

Table 1 Photovoltaic parameters of Type-I devices without an ETL, with PDINN, and with THA-I. The average PCE values were obtained from 20 devices

	V_{OC} [V]	J_{SC} [mA cm^{-2}]	EQE J_{SC}[mA cm^{-2}]	FF [%]	Best PCE [%]	PCE$_{avg}$ [%]
w/o ETL	0.766	24.865	23.50	62.51	11.93	10.69 (±0.70)
PDINN	0.877	26.491	25.39	77.75	18.08	17.61 (±0.31)
THA-I	0.877	26.695	25.66	78.68	18.41	18.05 (±0.23)

Furthermore, the change in surface potential induced by THA-I appears to occur similarly on the Ag electrode side (Fig. 2k). The UPS spectra in the secondary electron cutoff region, shown in Fig. 2k, reveal a substantial decrease in the WF of Ag from 4.71 eV to 3.87 eV after THA-I treatment.

If THA-I does not form a substantial physical layer, the question arises as to how it exists on the surface and whether it exists at all. To obtain direct evidence of the presence of atomic species related to THA-I on the surface of the BHJ layer and to investigate the working mechanism of THA-I in the OSCs, X-ray photoelectron spectroscopy (XPS) measurements were conducted under various conditions, including THA-I, Ag/THA-I, BHJ/THA-I, and BHJ/THA-I/Ag. Detailed conditions of each XPS sample are listed in Table S3 (SI). Fig. 3a and b show the XPS spectra of the I 3d and N 1s core levels, respectively. The I 3d spectrum exhibited two distinct 3d doublets, with peaks at high and low binding energies (BE) corresponding to I 3d$_{3/2}$ and I 3d$_{5/2}$, respectively. For THA-I, the peak positions of I 3d$_{3/2}$ and I 3d$_{5/2}$ appeared at 629.9 and 618.4 eV, respectively. The N 1s spectrum shows a single peak at 402.3 eV, corresponding to the N+ state of the THA-I cation. For THA-I on the Ag surface (Ag/THA-I), the I 3d$_{3/2}$ and I 3d$_{5/2}$ peaks shifted to slightly higher BE values of 630.5 and 619.0 eV, respectively, compared to those under the THA-I condition. These I 3d peak positions in Ag/THA-I suggest a chemical reaction between the iodides and Ag, leading to the formation of Ag–I bonds, consistent with prior reports on AgI.[35,36] In contrast, the N 1s peak in Ag/THA-I remained unchanged at 402.3 eV, indicating the absence of a reaction between the THA cations and Ag. This can be attributed to the steric hindrance properties of the THA cations.[37,38]

For THA-I on top of the BHJ layer (BHJ/THA-I), interestingly, the I 3d$_{3/2}$ and I 3d$_{5/2}$ peaks shifted to lower BE values of 629.5 and 618.0 eV, respectively. Furthermore, the N 1s spectrum of

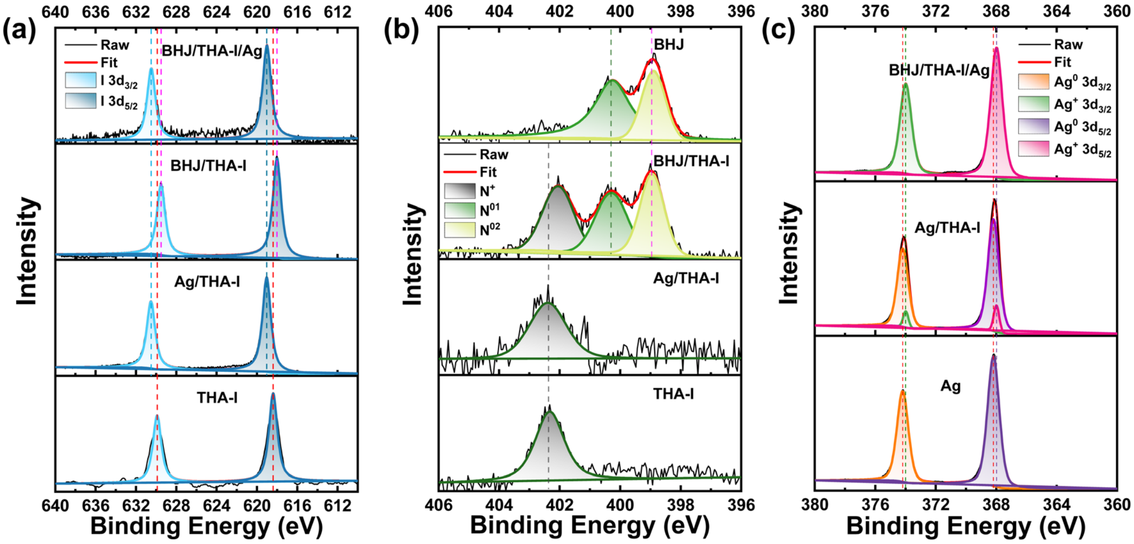

Fig. 3 Surface properties of THA-I N-type salt. (a) XPS spectra of the I 3d core levels for THA-I, Ag/THA-I, BHJ/THA-I, and BHJ/THA-I/Ag layers. (b) XPS spectra of the N 1s core levels for THA-I, Ag/THA-I, BHJ/THA-I, and BHJ layers. (c) XPS spectra of the Ag 3d core levels for Ag, Ag/THA-I, and BHJ/THA-I/Ag layers.

BHJ/THA-I was deconvoluted into three peaks, where the first peak at 402.0 eV corresponded to the N^+ state of the THA cations. The other two peaks, at 400.3 and 398.9 eV, corresponded to the N species within the BHJ layer, denoted as N^{01} and N^{02}, respectively. These N^{01} and N^{02} peaks exhibit a similar pattern to the N 1s spectra observed in the BHJ. Note that the acceptor L8-BO contains N species. We observed a shift to lower BE in both the I 3d and N^+ peaks in BHJ/THA-I compared to THA-I, which is probably due to differences in the electrostatic properties between the BHJ and Si substrate. The formation of AgI can be further confirmed under the BHJ/THA-I/Ag condition. Following the deposition of an extremely thin Ag layer (*ca.* 1 nm) onto the BHJ/THA-I surface, the I $3d_{3/2}$ and I $3d_{5/2}$ peaks of BHJ/THA-I/Ag shifted again, appearing at 630.5 and 619.0 eV, respectively, similar to those of Ag/THA-I. Importantly, it is worth emphasizing that the I 3d spectrum of BHJ/THA-I/Ag was identical to that of Ag/THA-I, providing compelling evidence of a reaction between the I anions and Ag. Confirmation of AgI formation can also be found in the observation of Ag 3d spectra (Fig. 3c). The Ag 3d spectrum exhibited two distinct doublets, with the peak at high BE corresponding to Ag $3d_{3/2}$ and the peak at low BE corresponding to Ag $3d_{5/2}$. The metallic Ag showed BE values at 374.18 and 368.18 eV, respectively, denoted as Ag^0 $3d_{3/2}$ and Ag^0 $3d_{5/2}$. The Ag 3d spectrum of BHJ/THA-I/Ag exhibited two distinct peaks at 373.98 and 367.98 eV, representing Ag^+ $3d_{3/2}$ and Ag^+ $3d_{5/2}$, respectively. This shift in the Ag 3d spectrum of BHJ/THA-I/Ag compared to those of BHJ/THA-I provides additional clear evidence of the formation of AgI, consistent with the study conducted by Kato *et al.*[39]

To summarize the XPS and UPS results, iodides strongly adhere to the Ag surface and form AgI. Simultaneously, the cations of THA-I are repelled from the Ag surface due to the polarity difference between their hexyl chains and the Ag surface.[40] As a result, iodides remain close to the Ag surface, while the cations of THA-I are positioned farther away, forming a dipole interface. The generated interfacial dipoles upwardly shift the E_{vac} at the Ag surface, leading to a reduction in the effective WF of the Ag electrode facing the BHJ. The combined XPS and UPS results are illustrated in an energy band diagram. When the OSC is made into an MSM structure without an ETL and HTL, the WF difference between the bottom electrode (ITO, WF: 4.2–4.7 eV) and the top electrode (Ag, WF: 4.3–4.7 eV) is small, resulting in a low internal built-in potential (V_{bi}), which provides limited driving force for charge dissociation and transport, as shown in Fig. 4a. Additionally, a large charge extraction barrier exists between the electrodes and the BHJ. However, when using Br-2EPSe SAM and THA-I (Fig. 4b), the WF difference between the ITO anode and Ag cathode increases, leading to a larger V_{bi}. Furthermore, the formation of dipoles at the interface between the BHJ and the electrodes lowers the energy barrier, allowing for efficient charge extraction. A more direct analysis of V_{bi} changes can be observed in the Mott–Schottky analysis shown in Fig. S5 (SI).

Next, we analyzed how the interfacial changes induced by THA-I affect charge dynamics, including generation, transport, and extraction. Since the effect of the Br-2EPSe SAM has already been fully analyzed in our previous paper,[33] we used a common Br-2EPSe SAM and focused solely on the effect of THA-I. Fig. 4c shows the photocurrent (J_{ph}) *versus* effective voltage (V_{eff}) curves for the OSCs without an ETL and with THA-I treatment. The analysis results are listed in Table S4 (SI). The OSC without an ETL exhibited an exciton dissociation efficiency of only 82.7% and a charge collection efficiency of 76.7%, significantly suppressing charge generation and extraction. In contrast, the OSC with THA-I treatment showed an exciton dissociation efficiency of 96.3% and a charge collection efficiency of 91.5%, which are better than those of the OSC with PDINN as the ETL. The improved exciton dissociation efficiency and charge collection

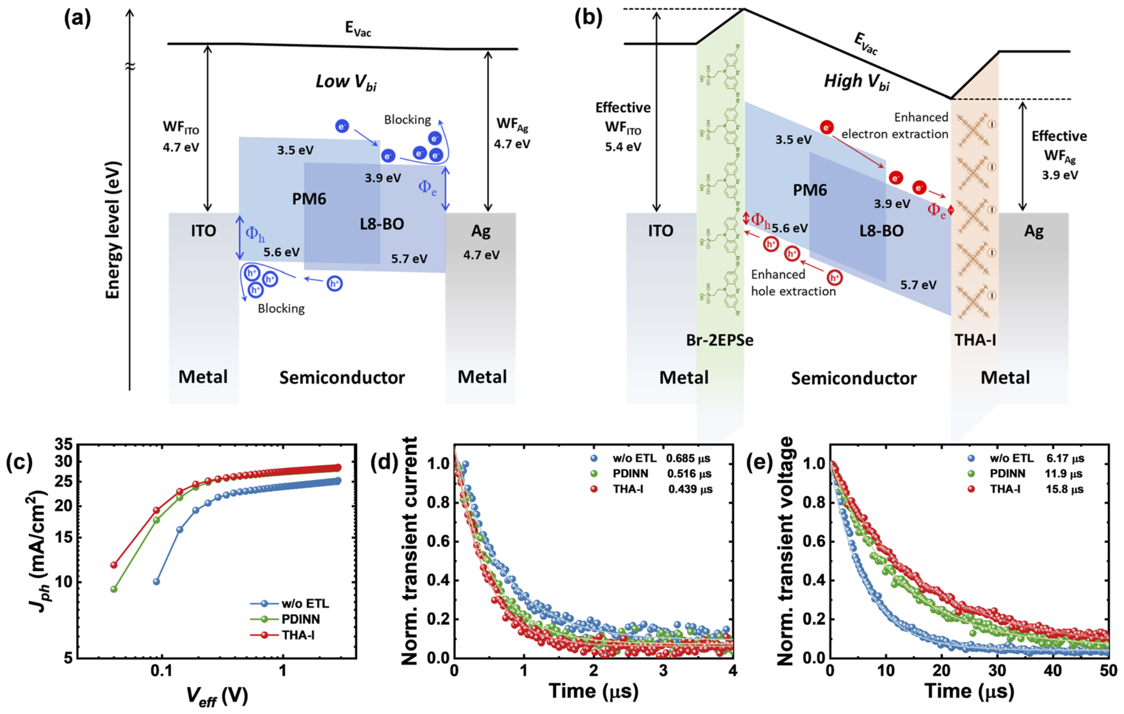

Fig. 4 Electronic properties of the THA-I N-type salt. (a) Energy band diagram of the MSM structure without hole and electron extraction interfaces. (b) Energy band diagram of Type-I (quasi-MSM). (c–e) J_{ph}–V_{eff} curves, transient photocurrent (TPC), and transient photovoltage (TPV) of Type-I devices without an ETL, with PDINN, and with THA-I, respectively.

efficiency are likely due to the effect of the larger internal potential. Fig. 4d and e show the transient photocurrent (TPC) and transient photovoltage (TPV) decays. From TPC and TPV, the carrier transport rate (transport time, τ_{trans}) and the charge carrier recombination rate (charge lifetime or recombination time, τ_{rec}) of OSCs can be determined using a single exponential decay model. In TPC (Fig. 4d), the device with THA-I treatment showed a shorter decay time compared to the devices without an ETL and with PDINN. This suggests that charges generated in THA-I treated devices arrive at the electrodes more quickly, which is consistent with the *J*–*V* results showing increased J_{SC}. This enhanced transport behavior is further supported by higher electron mobility extracted from electron-only devices, as determined by SCLC measurements (Fig. S7, SI). In TPV (Fig. 4e), the device with THA-I treatment exhibits a longer decay time, indicating that the recombination at the interface is reduced. Considering that the performance improvement in the solar cell with THA-I treatment was achieved through FF improvement, the TPV result showing a reduction in interfacial recombination is consistent with the *J*–*V* results. The improved charge extraction capability achieved by the THA-I treatment can also be confirmed by impedance spectroscopy (IS) analysis (see Fig. S8, SI).

In a nanoscratch test conducted to evaluate the adhesive interaction between the PM6:L8-BO layer and the Ag electrode, the PM6:L8-BO/Ag sample without an ETL exhibited the lowest critical adhesion force (F_c) of 1.12 mN (Fig. S9 and Table S5, SI). The sample with PDINN inserted between the PM6:L8-BO layer and the Ag electrode showed an F_c of 1.36 mN, which remained similarly low compared to the PM6:L8-BO/Ag sample without an ETL. In contrast, THA-I treatment on PM6:L8-BO improved the F_c between the PM6:L8-BO layer and the Ag electrode to 1.76 mN. This improvement is attributed to the formation of AgI *via* chemical bonding between the I^- ions of THA-I and the Ag surface, as confirmed by XPS results. The ionic bonding is likely to stabilize the interface between the PM6:L8-BO layer and the Ag electrode, potentially enhancing adhesion.

To assess the impact of THA-I treatment on device performance, we evaluated the long-term photostability and thermal stability of MSM Type-I devices. The normalized PCE and degradation trends over time are summarized in Fig. S11–S14 (SI). Under simulated 1 sun illumination (25 °C, 20% RH), MPP tracking of encapsulated devices showed that the THA-I-treated device retained 82.3% of its initial PCE after 500 hours, significantly outperforming the untreated device (27.5%), despite the simplicity of the interfacial treatment (Fig. S12, SI). As shown in Fig. S13 (SI), even without encapsulation, the THA-I-treated device exhibited superior thermal stability after 500 hours at 65 °C and 65% RH.

Type II: MSM device with P-type salt for holes & N-type salt for electrons

In Type-II devices, two different salts, rubidium-tetraphenylborate (Rb-TPB) and THA-I, were used to modify the hole extraction pathway and electron extraction pathway, respectively. Since Rb-TPB is also presumed to be layerless, it can be considered a true MSM from this Type-II onward. In this section, we compared two devices, one without a HTL and the

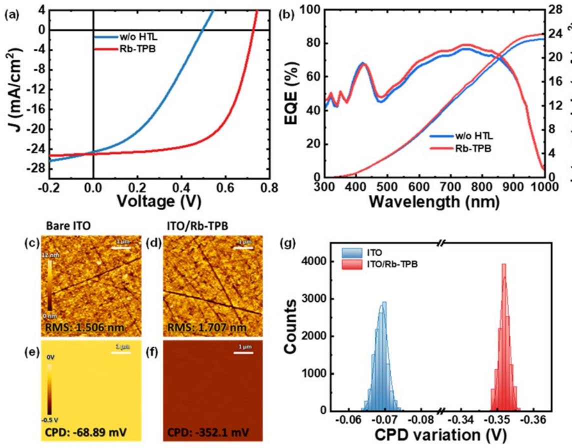

Fig. 5 Photovoltaic performance and characterization of Type-II devices. (a) J–V curves of Type-II devices measured under AM 1.5 G (100 mW cm^{-2}) illumination. (b) EQE spectra, (c and d) AFM surface morphology images, (e and f) KPFM surface potential images, and (g) contact potential difference measurements of bare ITO and ITO with Rb-TPB P-type salt, respectively.

other with Rb-TPB applied, to focus on the effects of Rb-TPB. Fig. 5a shows the J–V characteristic curves of a device without an HTL and a device using Rb-TPB treatment. The WF of the ITO surface treated with Rb-TPB did not match well with the PM6:Y6-based solar cells, and thus PTB7-Th and IEICO-4F were used as photoactive layer materials in this Type-II device (Fig. S20, SI). Detailed device optimization for Rb-TFB concentration is provided in Fig. S19 and Table S7 (SI). The solar cell without a HTL shows poor performance with a low FF and significantly depressed V_{OC}. However, in the case of solar cells with Rb-TPB treatment, the PTB7-Th: IEICO-4F solar cells exhibit performance levels comparable to those typically observed even without an HTL.

The surface properties of Rb-TPB-treated ITO (ITO/Rb-TPB) were examined using KPFM. No significant morphological differences were observed between the bare ITO surface (Fig. 5c) and the ITO/Rb-TPB surface (Fig. 5d). The surface potentials of bare ITO and ITO/Rb-TPB substrates were measured using KPFM, as shown in Fig. 5e and f. Similar to the THA-I case, Rb-TPB functions as a layerless modifier, altering only the surface properties. The CPD value shifted from −68.89 mV to −352.1 mV in a direction more favorable for hole transport, and the surface potential distribution became more uniform (Fig. 5e–g). Additionally, IS, TPV, and TPC analyses confirm a reduced charge recombination probability at the interface due to the presence of Rb-TPB (Fig. S21, SI). Notably, Rb-TPB demonstrates promising photovoltaic performance among the P-type salts we have examined and tested thus far. However, identifying P-type salts suitable for high-performance photoactive materials, such as the PM6:Y6 combination, remains a challenge.

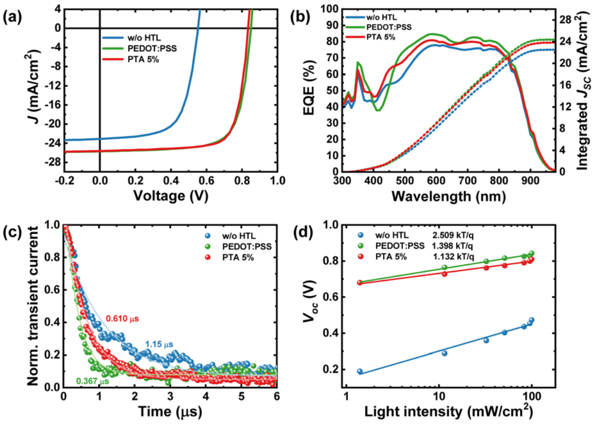

Fig. 6 Photovoltaic performance and characterization of Type-III devices. (a) J–V curves and (b) EQE spectra of Type-III devices. (c) TPC, and (d) light intensity dependence of V_{OC} for Type-III devices.

Type III: MSM device with PTA for holes & N-type salt for electrons

In Type-III devices, PTA was mixed into the photoactive material for simultaneous coating, naturally forming the hole extraction interface, while the electron transport interface was modified by introducing the THA-I salt. It was designed with one less coating step compared to the Type-II device, resulting in a more simplified fabrication process. Some aspects of HTL-free OSCs using PTA have already been reported in our previous studies.[41] Therefore, this manuscript will omit a detailed analysis of PTA and instead present only the basic performance results of the devices fabricated in combination with THA-I that is newly found in this work. Fig. 6a and b show the J–V characteristic and EQE curves of a device without an HTL and a device where 5% PTA was mixed with the PM6:Y6 photoactive solution and coated. For comparison, the results of a device using PEDOT:PSS as the HTL are also presented (detailed performance parameters are listed in Table S10, SI). In all three cases, THA-I was used in place of the ETL. The device using PTA showed a slight decrease in V_{OC}, but its overall performance was nearly similar to that of the device with the PEDOT:PSS HTL. This indicates that THA-I used at the electron transport interface is functioning properly, and PTA, which was simultaneously coated with the photoactive layer, is also working as intended. The slight performance degradation compared to devices using PEDOT:PSS as the HTL is believed to be due to the increased τ_{trans} through the photoactive layer, as shown in the TPC results in Fig. 6c. It is likely that residual PTA scattered throughout the photoactive layer acts as an obstacle to exciton generation, charge separation, and transport (see Fig. S27, S28 and Tables S11–S13, SI).

However, the interfacial recombination characteristics were observed to improve in the device using PTA. The charge recombination properties near open-circuit conditions were evaluated by monitoring the V_{OC} values as a function of the illuminated light intensity (Fig. 6d). In devices without a HTL, where the generated holes cannot be effectively extracted, a naturally high ideality factor (k_BT/q) was observed. Comparing the device using PEDOT:PSS with the device using PTA, the extracted ideality factor was 1.398 for the PEDOT:PSS-based HTL device. In contrast, the device using PTA exhibited a lower ideality factor of 1.132, indicating reduced recombination. This reduction in recombination was further confirmed by TPV measurements (Fig. S27b, SI) and intensity-modulated impedance spectroscopy (IMPS) measurements (Fig. S28, SI). However, incorporating PTA into the photoactive layer led to a slight reduction in the exciton generation rate (Fig. S27c and Table S11, SI) and a decrease in charge collection efficiency (Table S13, SI), contributing to a modest decline in overall device performance. Nevertheless, it is noteworthy that devices using PTA and THA-I (*i.e.*, without both the HTL and ETL) exhibited a performance level comparable to that of devices using PEDOT:PSS, demonstrating that this Type-III approach can serve as a simple and promising method for fabricating high-performance organic solar cells. Further optimizations are currently underway.

Scale up module device

The biggest advantage of HTL- and ETL-free MSM-structured solar cells is that it enables simplification of the fabrication process when applied to module production. We investigated whether the HTL- and ETL-free technology, implemented using THA-I and PTA, could simplify the module fabrication process. Fig. 5a presents a schematic diagram outlining the key steps typically involved in module fabrication. When utilizing a SAM and THA-I, which have no lateral charge transport characteristics, the damage protection layer and its patterning process can be omitted (Fig. 7b). A module can be fabricated by forming a SAM HTL on the ITO surface, depositing the photoactive layer, performing cell patterning, and treating the entire device surface with THA-I. THA-I was simply coated and dried without any patterning process, followed by the deposition of the top electrode. A photograph of the fabricated module and the *J*–*V* curve are shown in Fig. 7c and d, respectively. Unfortunately, the module using a SAM HTL did not show very good performance (Table S14, SI), as it is well known that the SAM encounters homogeneity issues when applied to large-area processes. We faced the same issue, and thus failed to produce a good performance module when incorporating a SAM into the module process. The module fabricated using PEDOT:PSS as the HTL showed better FF with an efficiency of 13.94%. Note that the total area of the fabricated module is 10 cm × 10 cm, and the active cell area is 54 cm^2 with 11 cells.

Applying the Type-III device fabrication method, which incorporates PTA into the photoactive layer, for module fabrication significantly simplifies the production process (Fig. 7e). A printing-based deposition process capable of directly patterning the desired shapes was experimentally implemented, enabling module fabrication in just three steps: photoactive layer + PTA printing, THA-I treatment, and cathode deposition. The Type-III device-based module, fabricated using this simplified three-step process, exhibits an MSM structure consisting of three layers: ITO, the photoactive layer, and the top electrode, as illustrated in the schematic cross-sectional image of the module in Fig. 7f. This structure arises because PTA and THA-I do not form distinct layers at the interface between ITO and the top electrode, yet they still facilitate efficient charge extraction without enabling lateral charge transport.

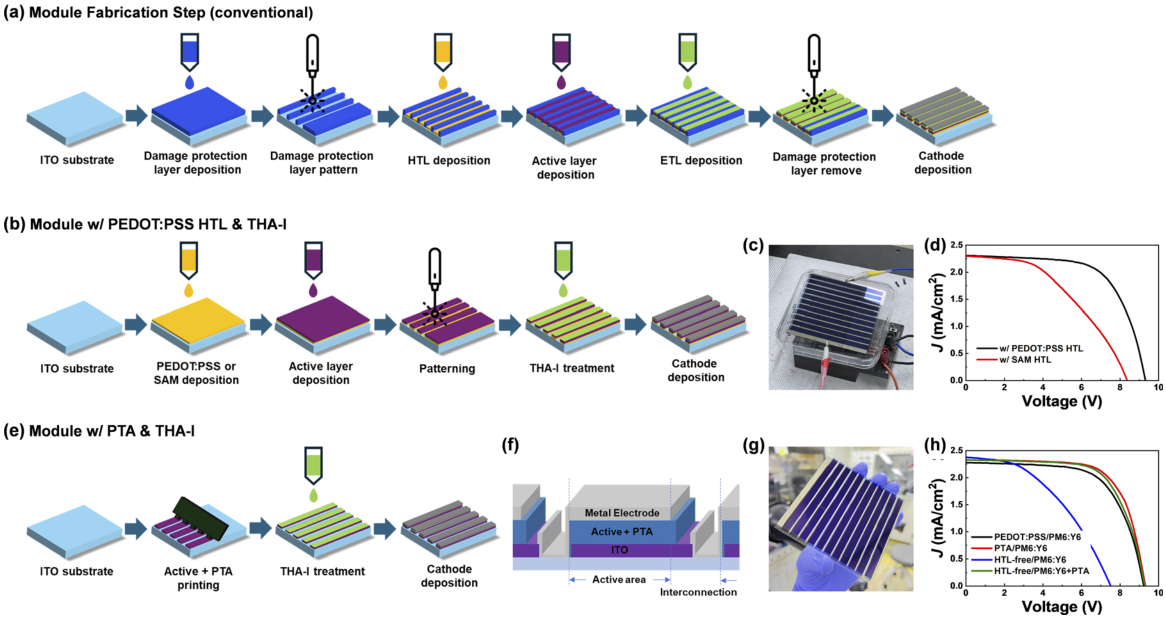

Fig. 7 Schematic diagram of the module fabrication process: the total module area is 10 cm × 10 cm, with an active cell area of 54 cm^2 comprising 11 cells. (a) Conventional module fabrication process (7 steps). Note that this is also a minimized process with simplified steps. In actual module fabrication, more than 12 steps are required, involving a more complex process. (b and c) Intermediate fabrication process (5 steps) and a photograph of the module using a PEDOT:PSS HTL and THA-I N-type salt. (d) *J*–*V* curves of the module with a PEDOT:PSS HTL or P-type SAM and THA-I N-type salt. (e–g) Simplified 3-step fabrication process, a module cross-sectional image, and a photograph of the Type-III module, respectively. (h) *J*–*V* curves of the Type-III module with a photoactive layer incorporating PTA and THA-I N-type salt. Modules with PTA or a PEDOT:PSS HTL were fabricated as control references.

Fig. 7g presents a photograph of the fabricated module, while Fig. 7h presents the *J*–*V* characteristic curves of the fabricated modules. The *J*–*V* characteristic curve of the PM6:Y6+PTA module exhibited slightly enhanced performance nearly identical to that of the module fabricated using the method shown in Fig. 7b, where PEDOT:PSS was employed as the HTL. For reference, the *J*–*V* curve of a module in which PTA was separately coated-similar to PEDOT:PSS-rather than blended into the photoactive layer is also shown. The transition toward HTL- and ETL-free OSCs aligns with the broader trend in solar technology toward reduced complexity, lower costs, and improved manufacturability. The findings reported in this study mark an initial step toward the development of solar cells with a fully simplified MSM structure. If a wider range of P-type and N-type salt materials are discovered or synthetically designed and integrated into the fabrication of more stable devices and modules, we believe this could significantly contribute to the large-scale production of next-generation organic solar cell modules.

Conclusions

We successfully demonstrated high-performance OSCs with a simplified MSM structure that eliminates the need for both the ETL and HTL. By utilizing small molecules such as THA-I, Rb-TPB and PTA, we effectively modified the interfacial properties, enhancing charge extraction and suppressing recombination. This resulted in PCEs exceeding 18%, comparable to those of conventional devices with an ETL and HTL. In particular, the Type-III module device demonstrated strong potential for scalability, offering a streamlined fabrication process suitable for large-area modules without sacrificing device performance. In conclusion, our study presents a groundbreaking approach that reduces manufacturing complexity and costs while improving or maintaining device performance. This novel strategy paves the way for more sustainable and scalable production of OSC modules, addressing critical challenges in the commercialization of OSCs.

Author contributions

S. C. designed and directed the research. The experiments were conducted by S. P., H. N. T., and H. L. under the supervision of S. C., and S. P., H. N. T., and H. L. contributed equally to this work. H. N. T. identified the THA-I salt and proposed the MSM structure basis. S. P., H. N. T., H. L., and M. J. fabricated and characterized devices of each MSM type. Y. W. L. synthesized Br-2EPSe and PDINN. H. Y. J. and E. C. J. performed and analyzed interfacial adhesion measurements. J. H. L., J. R., J. Y. K. and J. H. S. conducted XPS and UPS measurements and analyses. The manuscript was written by S. C., S. P., and H. N. T. All authors contributed to discussions about the manuscript and B. K. and D. C. L. provided advice on the research.

Conflicts of interest

There are no conflicts to declare.

Data availability

The data supporting this article are provided in the supporting information (SI). Supporting information: additional experimental details, device fabrication procedures, characterization data (AFM, KPFM, XPS, UPS, SCLC, IS, TPC/TPV), stability measurements, and supporting figures and tables. See DOI: https://doi.org/10.1039/d6el00010j.

Acknowledgements

This research was supported by the National Research Foundation of Korea (RS-2024-00465834, 2021R1A6A3A01088822, RS-2023-NR077279, and RS-2025-24523888). This research was supported by the “Regional Innovation System & Education (RISE)” through the Ulsan RISE Center, funded by the Ministry of Education (MOE) and the Ulsan Metropolitan City, Republic of Korea.(2025-RISE-07-001). This research was partially supported by the 2025 Future Technology Research Program of Hyundai Motor Company and Kia Corporation. This work was partially supported by Korea Southern Power Co., Ltd. (KOSPO) under Project No. PICQ480.

Notes and references

1 C. W. Tang, *Appl. Phys. Lett.*, 1986, **48**, 183.
2 G. Yu, J. Gao, J. C. Hummelen, F. Wudl and A. J. Heeger, *Science*, 1995, **270**, 1789.
3 A. C. Arias, M. Granström, D. S. Thomas, K. Petritsch and R. H. Friend, *Phys. Rev. B*, 1999, **60**, 1854.
4 F. Zhang, M. Johansson, M. R. Andersson, J. C. Hummelen and O. Inganäs, *Adv. Mater.*, 2002, **14**, 662.
5 C. J. Brabec, S. E. Shaheen, C. Winder, N. S. Sariciftci and P. Denk, *Appl. Phys. Lett.*, 2002, **80**, 1288.
6 V. D. Mihailetchi, P. W. M. Blom, J. C. Hummelen and M. T. Rispens, *J. Appl. Phys.*, 2003, **94**, 6849.
7 M. O. Reese, M. S. White, G. Rumbles, D. S. Ginley and S. E. Shaheen, *Appl. Phys. Lett.*, 2008, **92**, 053307.
8 V. Gupta, A. Ko Ko Kyaw, D. H. Wang, S. Chand, G. C. Bazan and A. J. Heeger, *Sci. Rep.*, 2013, **3**, 1965.
9 C. Sun, Z. Wu, Z. Hu, J. Xiao, W. Zhao, Ho- Wa Li, Q.- Ya Li, S.-W. Tsang, Y.-X. Xu, K. Zhang, H.-L. Yip, J. Hou, F. Huang and Y. Cao, *Energy Environ. Sci.*, 2017, **10**, 1784.
10 V. Shrotriya, G. Li, Y. Yao, C.-W. Chu and Y. Yang, *Appl. Phys. Lett.*, 2006, **88**, 073508.
11 H.-H. Liao, Li-M. Chen, Z. Xu, G. Li and Y. Yang, *Appl. Phys. Lett.*, 2008, **92**, 173303.
12 E. L. Ratcliff, J. Meyer, K. X. Steirer, N. R. Armstrong, D. Olson and A. Kahn, *Org. Electron.*, 2012, **13**, 744.
13 C. E. Small, S. Chen, J. Subbiah, C. M. Amb, S.-W. Tsang, T.-H. Lai, J. R. Reynolds and F. So, *Nat. Photon.*, 2012, **6**, 115.
14 K. Lee, J. Y. Kim, S. H. Park, S. H. Kim, S. Cho and A. J. Heeger, *Adv. Mater.*, 2007, **19**, 2445.
15 B. Bob, T.-B. Song, C.-C. Chen, Z. Xu and Y. Yang, *Chem. Mater.*, 2013, **25**, 4725.
16 A. Ko Ko Kyaw, D. H. Wang, V. Gupta, J. Zhang, S. Chand, G. C. Bazan and A. J. Heeger, *Adv. Mater.*, 2013, **25**, 2397.

17 Y. Zhou, C. Fuentes-Hernandez, J. Shim, J. Meyer, A. J. Giordano, H. Li, P. Inget, T. Papadopoulos, H. Cheun, J. Kim, M. Fenoll, A. Dindar, W. Haske, E. Najafabadi, T. M. Khan, H. Sojoudi, S. Barlow, S. Graham, J.-L. Brédas, S. R. Marder, A. Kahn and B. Kippelen, *Science*, 2012, **336**, 327.

18 F. Huang, H. Wu, D. Wang, W. Yang and Y. Cao, *Chem. Mater.*, 2004, **16**, 708.

19 L. Hu, F. Wu, C. Li, A. Hu, X. Hu, Y. Zhang, L. Chen and Y. Chen, *Macromolecules*, 2015, **48**, 5578.

20 J. Yao, B. Qiu, Z.-G. Zhang, L. Xue, R. Wang, C. Zhang, S. Chen, Q. Zhou, C. Sun, C. Yang, M. Xiao, L. Meng and Y. Li, *Nat. Commun.*, 2020, **11**, 1.

21 M. Zi, X. Chen, S. Tan, C. Weng and B. Zhao, *Chem. Eng. J.*, 2022, **443**, 136455.

22 S. Park, M. J. Cha, J. H. Seo, J. Heo, D. C. Lim and S. Cho, *ACS Appl. Mater. Interfaces*, 2018, **10**, 41578.

23 J. Troughton, A. Seitkhan, M. Neophytou, F. H. Isikgor, N. Gasparini, X. Song, Y.-H. Lin, T. Liu, H. Faber, E. Yengel, J. Kosco, M. F. Oszajca, B. Hartmeier, M. Rossier, N. A. Lüchinger, L. Tsetseris, H. J. Snaith, T. D. Anthopoulos, S. De Wolf, I. McCulloch and D. Baran, *Energy Environ. Sci.*, 2020, **13**, 268.

24 L. Hu, J. Song, X. Yin, Z. Su and Z. Li, *Polymers*, 2020, **12**, 145.

25 M. Wu, B. Ma, S. Li, J. Han and W. Zhao, *Adv. Funct. Mater.*, 2023, **33**, 2305445.

26 P. Rathore and J. D. Schiffman, *ACS Eng. Au*, 2023, **3**, 527.

27 L. V. Kayser and D. J. Lipomi, *Adv. Mater.*, 2019, **31**, 1806133.

28 A. M. Nardes, R. A. J. Janssen and M. Kemerink, *Adv. Funct. Mater.*, 2008, **18**, 865.

29 A. Inoue, H. Yuk, B. Lu and X. Zhao, *Sci. Adv.*, 2020, **6**, eaay5394.

30 T. Nagata, S. Oh, T. Chikyow and Y. Wakayama, *Org. Electron.*, 2011, **12**, 279.

31 B. J. Bruijnaers, E. Schiepers, C. H. L. Weijtens, S. C. J. Meskers, M. M. Wienk and R. A. J. Janssen, *J. Mater. Chem. A*, 2018, **6**, 6882.

32 A. Ullah, K. H. Park, H. D. Nguyen, Y. Siddique, S. F. A. Shah, H. Tran, S. Park, S. I. Lee, K.-K. Lee, C.-H. Han, K. Kim, S. Ahn, I. Jeong, Y. S. Park and S. Hong, *Adv. Energy Mater.*, 2022, **12**, 2103175.

33 A. Ullah, K. H. Park, Y. Lee, S. Park, A. B. Faheem, H. D. Nguyen, Y. Siddique, K.-K. Lee, Y. Jo, C.-H. Han, S. Ahn, I. Jeong, S. Cho, B. Kim, Y. S. Park and S. Hong, *Adv. Funct. Mater.*, 2022, **32**, 2208793.

34 J.-H. Lee, J. Kim, G. Kim, D. Shin, S. Y. Jeong, J. Lee, S. Hong, J. W. Choi, C.-L. Lee, H. Kim, Y. Yi and K. Lee, *Energy Environ. Sci.*, 2018, **11**, 1742.

35 C. A. Strydom, J. F. van Staden and H. J. Strydom, *Electroanalysis*, 1991, **3**, 197.

36 Q. Yan, Y. Fu, Y. Zhang, H. Wang, S. Wang and W. Cui, *Sep. Purif. Technol.*, 2021, **263**, 118389.

37 Y. Miao, Y. Chen, H. Chen, X. Wang and Y. Zhao, *Chem. Sci.*, 2021, **12**, 7231.

38 Y. Hiruta, T. Watanabe, E. Nakamura, N. Iwasawa, H. Sato, K. Hamada, D. Citterio and K. Suzuki, *RSC Adv.*, 2014, **4**, 9791.

39 Y. Kato, L. K. Ono, M. V. Lee, S. Wang, S. R. Raga and Y. Qi, *Adv. Mater. Interfaces*, 2015, **2**, 1500195.

40 Y. Chen, S. Wang, L. Xue, Z. Zhang, H. Li, L. Wu, Y. Wang, F. Li, F. Zhang and Y. Li, *J. Mater. Chem. A*, 2016, **4**, 19189.

41 M. Jahandar, N. K. Wardani, H. Lee, J. Heo, Y. H. Kim, S. Cho, S. Kim and D. C. Lim, *Chem. Eng. J.*, 2024, **481**, 148482.